Buckling due to external pressure of a composite tube measured by Rayleigh optical backscatter reflectometry and analyzed by finite elements

Eivind Hugaas, Nils Petter Vedvik and Andreas T. Echtermeyer

Norwegian University of Science and Technology, NTNU

Trondheim, Norway

Abstract

There is a growing interest in replacing steel tubes that operate in high pressure and high temperature environments with composite tubes. Such applications can include drilling risers and drill strings for the offshore oil industry. Replacing steel with composites in such applications will greatly reduce the weight of the equipment and require less buoyancy elements built into the structures.

This paper seeks to investigate how composite tubes behave when submerged and how optical fibers can be used as a health monitoring system for such applications utilizing Rayleigh optical backscatter reflectometry.

A glass fiber filament wound tube of 100 mm inner diameter and 600 mm length with a layup of approximately $[89°, \pm 12.7°, \pm 45°]$ was exposed to external hydrostatic pressure in an autoclave. Optical fibers glued to the outer surface of the tube were used to measure strain during testing. A strain field reading was carried out every 0.5 bar pressure increase and correlated well with strain fields from a FE analysis of the tube. The FE analysis predicted buckling at 4.33 bar assuming no material failure; however, the tube buckled at 3.5 bar due to a sudden stiffness reduction from material failure. The optical fibers could detect the early failure and functioned well as a health monitoring system.

Keywords

Rayleigh backscatter, strain measurement, composite tubes, buckling, external pressure, finite element analysis.

Introduction

Composite tubes see many different applications today due to high stiffness and strength combined with relatively low weight. There is an increasing interest in replacing steel tubes that operate in high pressure and high temperature environments with composite tubes [1]. Such applications can include drilling risers and drill strings for the offshore oil industry [2]. Replacing steel risers and steel drill strings with composite tubes will greatly reduce the weight of the equipment, and will have the benefit of requiring less buoyancy elements built into the structures. Although composite tubes have been used extensively as pressure pipes, little use has been seen when the greater pressure is from external pressure, as is often one of the design cases at deep waters. In order for composite tubes to be qualified for such environments they need to be thoroughly tested to qualify not only the material, but also the analysis tools, design methodology and in some cases health monitoring systems [3], [4].

Relevant work on composite pressure vessels over the past 20 years has been summarized by P.Davies et.al [5]. The paper includes a wide range of topics, from end closures on tubes to NDT and material investigations. Of particular interest, was addressing measurements of hoop strains during bifurcation buckling of a thick walled deep sea composite cylinder [6]. Davies instrumented a 1.25 m long cylinder with 500 mm inner diameter and 40 mm wall thickness with 18 strain gauges around the middle circumference plus additional strain gauges around other circumferences. The gauges were able to detect a two lobe buckling pattern when the tube buckled at 610 bar. As such, Davies achieved a semi continuous strain field, however with extensive work mounting the gauges.

Utilizing a different measurement approach than strain measurement is the work by M. Pinto et. al. [7]. Pinto used visual inspection with cameras to measure the displacement of the outer surface of submerged composite tubes during bifurcation buckling. The tubes were of comparable geometry as in this paper. The measurements provided detailed info on how the buckling and different failure modes propagated over time. Pinto found that the tubes buckled with a two lobe shape and underwent very high deformations during buckling, causing matrix cracking and some fiber fracture.

The work by D. Choqueuse et. al. [8] is also relevant in the context of proving the functionality of optical fibers applied to submerged pressurized structures. Choqueuse embedded optical Fiber Bragg Gratings (FBG) into a Carbon Fiber Reinforced Polymer (CFRP) layer filament wound onto a steel tube before exerting the tube to external hydrostatic pressure in an autoclave. The study concluded that the fibers performed well up to 200 bar, where after the fibers likely sustained damage at the micro level. Choqueuse also concluded that prediction of the buckling behavior of submerged composite tubes is difficult.

K. Lim et. al. [9] conducted a comparable experiment on a PVC tube with internal pressure. Lim Investigated to what degree PVC tubes deform non-uniformly when filled with water and added internal pressure. Lim used optical fibers glued circumferentially on the outer surface at several cross sections along the length of the tube and measured the strain using Brillouin backscatter. The tube's outer diameter was 315 mm with a wall thickness of 6 mm and a length of 5.83 m. The optical fiber managed to pick up an elliptical deformation pattern once filled up due to the water self-weight. The elliptical shape decreased as the internal pressure increased, as one would expect. It was concluded that optical fiber glued to the outer surface of a PVC tube is able to capture the correct deformation pattern occurring when the tube is filled up, and also under pressure.

The work in this paper seeks to get a step closer to understanding the behavior of composite tubes when subjected to external pressure. To investigate the behavior, Finite Element Analysis (FEA) in combination with health monitoring during testing by the use of optical fibers utilizing the Rayleigh optical backscattering, was carried out. Besides serving as a tool to increase understanding of the mechanical behavior, FEA was chosen as the most convenient tool for verification of the strain field measurements.

Materials and methods

Tube design and fabrication

The glass fiber reinforced polymer tube was manufactured using filament winding. The fiber was HiPer-Tex W2020 from 3B [10] and the epoxy was EPIKOTE Resin MGS RIMR 135 with curing agent EPIKURE Curing Agent RIMH 137. The epoxy and curing agent were mixed and cured according to the corresponding datasheet [11]. The inner diameter of the tube was 100 mm and the length of the tube was 600 mm, wound with the layup $[89°, \pm 12.7°, \pm 45°]$ with the hoop (89°) as the innermost layer. The thickness of the tube was measured with a micrometer to be 1.675 mm and the thickness of the individual layers was found through microscopy of the cross section. The layer thicknesses are reported in Table 1.

The fiber volume fraction of the tube was found to be 0.6 obtained by burn-off tests according to ASTM D3171 – 15 [12].

Due to the nature of composite materials, the properties vary with the production method. A filament winded tube will have different elastic constants and strengths compared to a vacuum infused plate with the same fiber and epoxy.

The material properties of the tube were taken from previous work by G. Perillo [13] on tubes using identical constituent materials. Perillo combined force/displacement curves from experiments of a point load on a short section of tube with a FEA by tuning the material data to achieve good correlation between FEA and experiment. The data had to be corrected for a change in volume fraction from 0.62 to 0.60. The same correction formulas as given in [13] were used. It should be noted that the corrections were minimal due to the small difference in volume fraction. The material properties are reported in Table 2.

Table 1 Measured thickness in the microscopy and layup of the FE model.

Orientation (winding angle)	Measured thickness (mm)	FEM* ply number	FEM* ply thickness (mm)
89°	0.263	1	0.26260
±12.7°	0.710	2 – 9	0.08875 (0.710 total)
±45°	0.702	10 – 17	0.08775 (0.702 total)

**Finite Element Model*

Table 2 Material Properties, E1 is scaled with a volume fraction of 0.60 as opposed to 0.62, which the original data from G. Perillo [13] assumed.

Parameter	Scaled value, (unscaled value)	Unit
E_1	37.5 (38.6)	GPa
E_2	11.0	GPa
v_{12}	0.3	-
G_{12}	3.07	GPa

FE model and analysis

The optical fiber strain fields were compared with FE analyses for a greater understanding of the buckling behavior. Seeing as visual inspection of the tube or introduction of other strain measurement technologies would be very difficult to implement inside the autoclave, FEA also served as a viable way to verify the functionality of the optical fiber when submerged.

Abaqus/CAE 6.12-1 was used to model and analyze the tube. The tube was modeled as a shell profile of 600 mm length with 100 mm inner diameter using SR4 shell elements having an element size of 2.0 mm. Abaqus' Composite Layup with Conventional Shell was used together with the scaled (only E_1) material properties in Table 2. In order to model the tube's ±12.7° and ±45° layers as closely as possible, eight balanced layers were used for each winding angle. The hoop (89°) layer; however, is not a balanced layer and was therefore modelled as a single layer. The layup is reported in Table 1.

A mesh sensitivity analysis, Table 3, with respect to linear buckling showed a minor influence on the buckling pressure or the first buckling mode, with all mesh sizes having the two-lobe buckling shape schematically shown in Figure 1.

Table 3 Mesh Sensitivity Analysis.

Mesh size (mm)	Buckling pressure (bar)	Buckling shape
2.0	4.7598	Two-lobe
8.0	4.8091	Two-lobe
16.0	4.9379	Two-lobe

A length sensitivity investigation was carried out by running linear buckling analyses of tubes having lengths ranging from 200 mm to 1500 mm The results are summarized in Figure 2. For tubes shorter than 500 mm the first buckling mode changes from two-lobe to a three-lobe shape. For even shorter tubes, the amount of lobes in the first buckling mode's shape increases, as indicated with the four-lobe pattern in the graph. For lengths exceeding 1000 mm the buckling pressure converges towards an infinitely long tube. It should be noted that the linear analyses were run with the same boundary conditions as for the 600 mm long tube. For shorter tubes, the relative stiffness contribution from the end caps is likely different and closer to a fixed constraint, making for a stiffer structure and higher buckling pressure for shorter tube lengths.

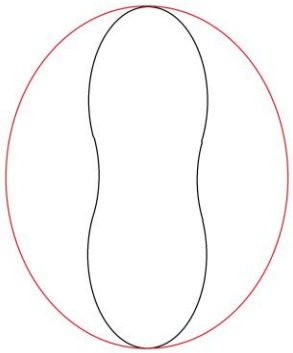

Figure 1 Schematic showing the principle of the two-lobe buckling shape (black) and the tube as modelled elliptic (red) to initiate nonlinear deformation with the Riks analysis method.

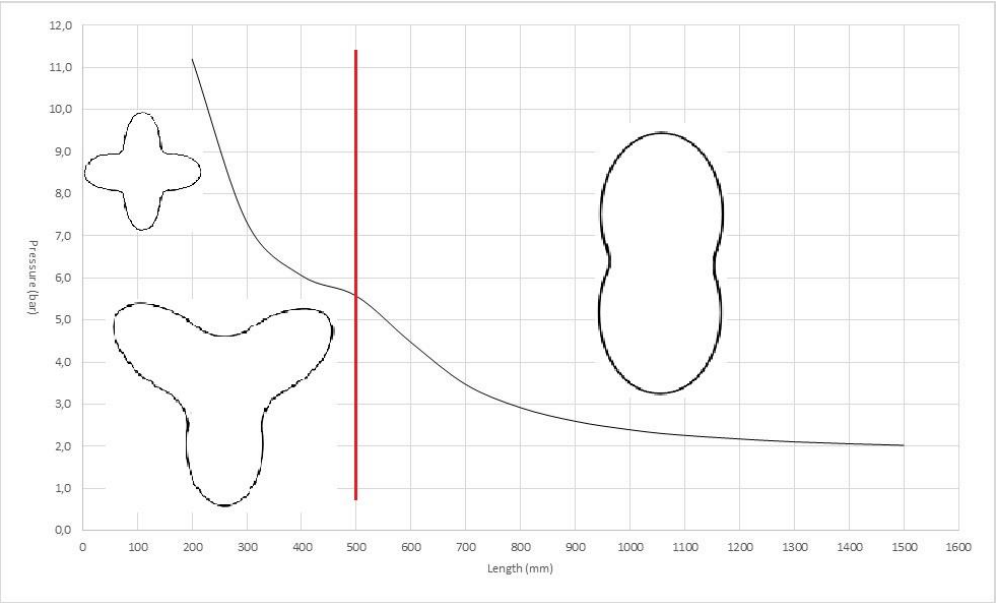

Figure 2 Length sensitivity investigation based on running several linear buckling analysis at different lengths. For tubes shorter than 500 mm (red line), the first buckling mode's shape changes to three-lobe, and for even shorter tubes the amount of lobes increases.

While a linear buckling analysis is an efficient method for estimating the buckling pressure as well as the mode and shape given ideal conditions, it does not provide any information about the post-buckling deformations. Therefore, the numerical study was extended using the Riks analysis method. While conventional nonlinear analyses have the loads added incrementally according to prescribed functions, the Riks method increments all loads automatically as part of the solution by the same factor using the Load Proportionality Factor (LPF). The concept of LPF implies that the method is limited to cases where all loads are linearly related to the same governing factor, such as hydrostatic pressure. A conventional nonlinear analysis is not able to capture the structural response in cases where the tangential structural stiffness becomes negative, such as during buckling. The Riks analysis method however, increments the load through the LPF automatically until equilibrium is found, also if that means reducing the load, which is needed if the tangential structural stiffness becomes negative. This means that the buckling pressure in a Riks analysis is where the LPF peaks and is as such not a direct output from the analysis, but is found through looking through the LPF history. To give the analysis a starting point, the size of the first LPF increment is given by the user, where after the Riks analysis method increments the LPF automatically [14], [15]. If a submerged tube is modelled as perfectly circular without any defects (ideal conditions) and analyzed with the Riks analysis method or in a general nonlinear analysis, instability and buckling will not occur, as the deformation will be stable. To initiate instability, the tube was modelled as slightly elliptic. The elliptic shape compared to the two-lobe buckling shape is schematically shown in Figure 1. Besides initiating instability, the degree of ovality in the FE model was tuned to make the FEA strain fields correlate well with the optical fiber strain fields. For more work on using ovality as a parameter to achieve good correlation between FEA and optic fiber strain fields on thin walled tubes exerted to external hydrostatic pressure, see the work by E. Hugaas [16]. This approach shows that the strain fields from the optical fibers can be used to optimize the FEA and improve the modeling techniques. Using this method, the ovality in the FE model becomes a parameter describing the general production quality of the tube, including other possible variations than the geometric ovality.

The end caps of the tube were considered as perfectly rigid, enabling a simplified constraint of the ends using kinematic coupling to reference points. The tube's ends were both pinned (freely supported) to two reference points set one at each end of the tube along the central axis using rigid body constraints to model the end caps. This implies that the ends were free to relative rotation, but not relative translation. Besides the rigid body constraints, one side was constrained to absolute translation in all directions of the cylindrical coordinate system, hindering also rotation around the longitudinal axis. This was done to keep the amount of DOFs down to avoid potential singularities in the global stiffness matrix. Figure 3 shows schematically how the tube was constrained. The tube had an external pressure of 10 bar (1 MPa) applied on the outer surface, as well as a point load of 8364.68 N applied at one end to simulate the pressure on the end caps, both loads are visible in Figure 3. The force of 8364.68 N was calculated by multiplying the pressure with the projected area, as shown in Equation 1.

$$F(t) = (\pi \cdot (r + t)^2 \cdot 10\ bar) = (\pi \cdot (50\ mm + 1.6\ mm)^2 \cdot 10\ bar) = 8364.68\ N \quad (1)$$

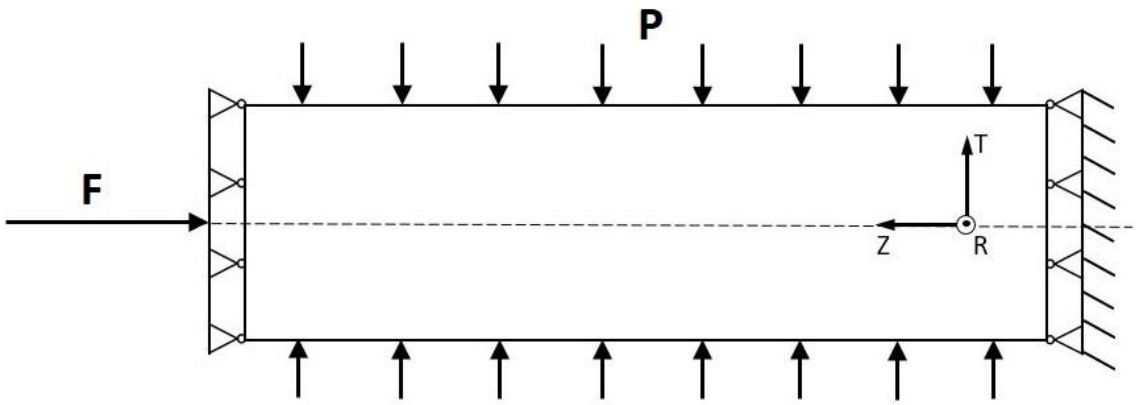

Figure 3 Schematic showing the tube as constrained with all loads applied. Also visible is the cylindrical coordinate system used.

Principle of strain measurement using the OBR method

The strain measurements were obtained using Luna Technologies' Optical Backscatter Reflectometer 4600 (OBR 4600) utilizing Rayleigh backscatter in a standard telecom optical fiber. Rayleigh backscattering is caused by light emitted into the fiber being reflected on natural irregularities in the fiber. In the OBR 4600 a coherent Optical Frequency Domain Reflectometer (OFDR) is used to emit light and direct the reflected light. The OFDR works by emitting light with a variable frequency into a March-Zender interferometer. The interferometer works by splitting the light from the laser source into the measuring fiber and into a reference fiber terminating in a detector. The reflected light from the fiber is transmitted back into the reference fiber before it enters the detector. Light from the detector is converted into a Fast Fourier Transformation graph (FFT) by the OBR 4600. The FFT acts as a fingerprint of the fiber and is only altered if there is a change in external conditions (strain or temperature). The greater the frequency in the FFT, the further away from the transmitter is the point at where the reflected light comes from and the amplitude in the FFT depends on the nature of the irregularity where the light was backscattered. To have a reference; a zero strain fingerprint, an FFT has to be recorded prior to measuring [17]. The gauge length and the spatial resolution is chosen based on compromising what gives the smoothest strain field curves without overlooking any strain variations critical for the investigation in question. The smallest spatial resolution and gauge length is in the millimeter range and is for most engineering applications not limited by the OBR 4600, but by the nature of the strain field to be

monitored. Additionally, the OBR 4600 is capable of live monitoring of strain, which is very advantageous for health monitoring [17].

The OBR 4600 technology can be categorized as a Distributed Fiber Optic Sensing (DFOS) technology, implying that it uses an array of sensors along the length of the fiber. Other DFOS technologies includes FBG, as used by Choqueuse presented in the introduction. With FBG the location of the sensors are set by modifying the fiber itself in advance and the amount of sensors per fiber is typically limited to ten, much less than with the OBR technique. Closer in functionality to utilizing the Rayleigh backscattering compared to FBG is using the Raman backscattering or the Brillouin backscattering, as used in Lim's work presented in the Introduction. The Rayleigh, Brillouin and the Raman backscattering rely on different interaction mechanisms between the emitted light and the fiber, with the Rayleigh backscattering giving the most intense backscatter [18]. The result is that both the Raman and the Brillouin backscattering gives a much lower available spatial resolution due to the lower intensity. As an example, Lim used 100 mm sensor spacing, giving at best a semi continuous strain field with the risk of not picking up critical variations in strain in between the gauges. The main advantage with utilizing the Raman or Brillouin backscattering is that measuring over fiber lengths up to several kilometers is possible, whereas the OBR 4600 currently is limited to 70 m maximum fiber length without compromising the spatial resolution [17]. It is important to note that the maximum fiber length when using the Rayleigh backscattering is only limited by data processing power and that 70 m does not represent a physical boundary [17].

Verification of the functionality and performance of the OBR 4600 with optical fiber applied to composites was investigated by M. Haaheim [19]. Haaheim embedded optical fiber into hand layup CFRP structures to thoroughly test the performance and strain measuring accuracy compared with FEA and other more traditional strain measurement methods. Haaheim concluded that the OBR 4600 corresponded well with both FEA and other methods, as also found and verified in this paper.

J. H. L Grave. et. al. [20] further verified the functionality and performance of the OBR 4600. Grave concluded that the technology offered an excellent solution for measuring strain in non-homogeneous strain fields.

Experimental setup of optical fibers

A single fiber with a diameter of 165 micron was glued on to the tube with cyanide optical fiber glue at three locations with 150 mm longitudinal spacing, as shown in Figure 4, thus only measuring hoop strain. The grey blocks seen in Figure 4 is Styrofoam taped lightly to the tube to keep the fiber from touching the internal walls of the autoclave. Between the measurement locations the fiber was left free, unglued, so as not to cause any disturbance. To smoothen the surface of the tube before applying the optical fiber, it was sanded with 400 grit sand paper. A close up picture of the fiber glued onto the tube can be seen in Figure 5. An isolated signal fiber was joined to the measurement fiber with a fiber heat-shrink joint after the last turn, as can also be seen in Figure 5. The joint was submerged during testing. The signal wire exited the autoclave through a watertight T-fitting on the pressure supply line, shown in Figure 6. To ensure a consistent zero strain measurement at zero pressure, the zero strain fingerprint was read prior to submerging the tube. During post-processing of the data from the fiber, the gauge length was set to 5 mm and the spatial resolution was set to 1 mm, giving 4 mm overlap of the virtual strain gauges.

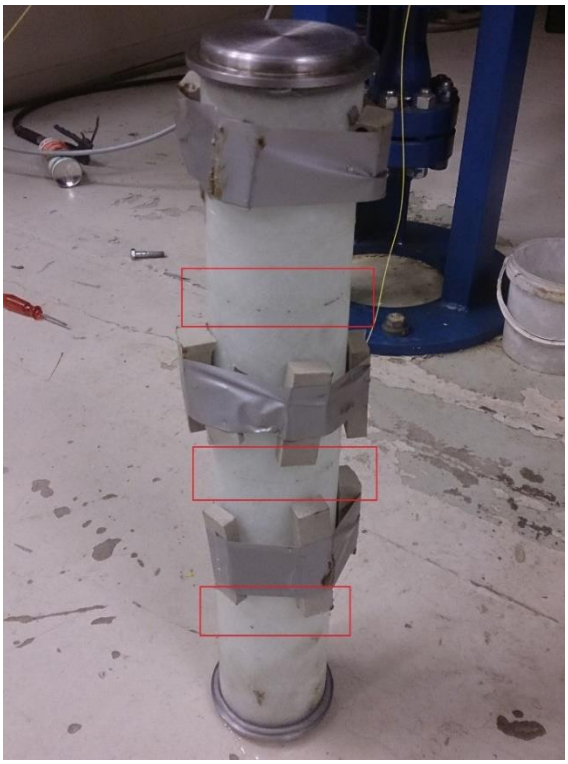

Figure 4 Tube with end caps and fiber protection (Styrofoam) glued and taped lightly onto the tube. The red squares outlines the fiber at 150 mm (bottom), 300 mm (middle) and 450 mm (top).

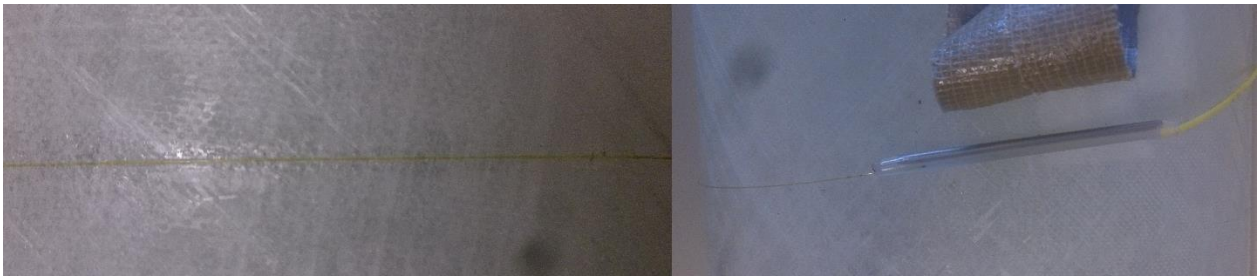

Figure 5 Close up of the optical fiber glued onto the tube (left) and the fiber heat-shrink tube (right) joining the signal wire and the optical fiber.

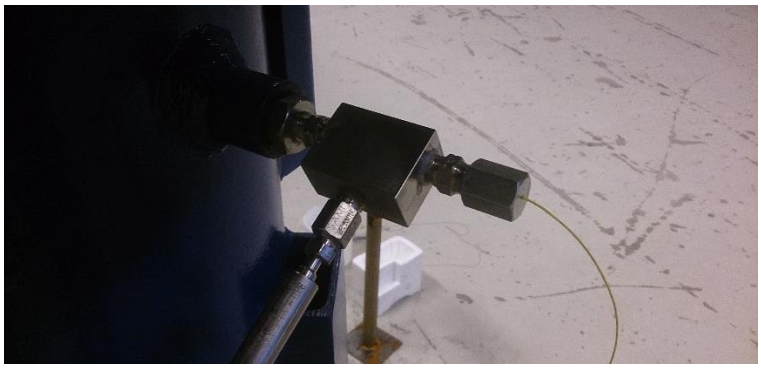

Figure 6 T-fitting on the pressure supply line on the autoclave with the fiber escaping through an end cap made watertight with silicon.

Results

In this section, the observations from the test and the results from the FEA are given. See the Discussion section for correlation of failure modes and buckling pressure with test and FEA results.

The pressure in the autoclave was increased in intervals of 0.5 bar and an optical fiber strain reading was carried out at each load increment. The pressure stopped increasing above 3.5 bar even though the pump was still running, indicating a leakage of the tube. The leakage, once initiated, only acted at pressures above 3.0 bar, making any pressure above 3.0 bar unstable and unsustainable. After the test there was however no visible failure on the tube indicating leakage. The temperature of the water was constant throughout the test at about 7 °C, so the measured strain was not in any way affected by temperature change, see [21] for effects of temperature on optical fiber. Figure 7, Figure 8 and Figure 9 show the optical fiber and FEA strain fields up to 3.5 bar, but does not include any measurements after the pressure dependent leakage occurred. One optical fiber strain reading was carried out after the leakage occurred, but after having bled off the pressure to 2.3 bar. For the 150 mm and 300 mm locations, the noise in the 2.3 bar strain fields was too severe to serve any use, but the strain field at 450 mm was better and a smoothed version can be seen in Figure 10. The raw 2.3 bar strain field at 450 mm (not smoothed) has been included to showcase the extent of the noise and can be seen in Figure 11.

The correlation between the FEA and the optical fiber strain fields for corresponding pressures is generally good. Because the Riks analysis method increments the LPF automatically, some of the analysis frames are at a slightly different pressure than the experimental pressure of which they are compared with. This is evident at the 3.5 bar test pressure compared with the Riks 3.41 bar frame, yielding 0.09 bar difference in pressure. An example of a good correlation both with regards to the strain field and the pressure is at 1.5 bar from the middle (300 mm) of the tube; indicated with yellow color in Figure 7, having good correlation with the yellow dashed FEA strain field at 1.52 bar. An ovality of 0.46 % of the nominal diameter (100 mm) was found to give the best correlation between the FEA and the optical fiber strain fields. 0.46 % ovality means that 0.46 mm (0.46 % x 100 mm = 0.46 mm) was subtracted and added to the minor and major diameter of the ellipse in the extrusion sketch respectively. Using established definitions of ovality this equates to 0.92 %; however, to be consistent with prior work by E. Hugaas [16] using ovality as a matching parameter for FEA, the stated definition is used here.

The Riks analysis method gave a peak LPF value of 0.433, equivalent to a pressure of 4.33 bar. This value is slightly below the 4.76 bar found by linear buckling analysis. The deviation between the two analyses was expected due to the elliptic shape of the tube in the Riks analysis compared to the ideal circle shape in the linear buckling analysis. Due to the reported leakage, the pressure in the tube never reached the FEA buckling pressure.

For visual reference of the deformation, Figure 12 shows the radial displacement of the tube at 3.41 bar in the FEA with a maximum absolute radial displacement of -0.79 mm. Also visible is the starting point for the path in the strain graph at 300 mm indicated by the black dot, the starting point for the 150 and 450 mm paths are along the same longitudinal axis. The tube's two-lobe buckling shape can be seen in the deformation plot with the creases in blue and lobes in red. It is also clearly present in the strain graphs with the "valleys" in the graphs being the creases and the two distinct peaks being the lobes. The two-lobe shape occurred as expected from the length sensitivity investigation in Figure 2.

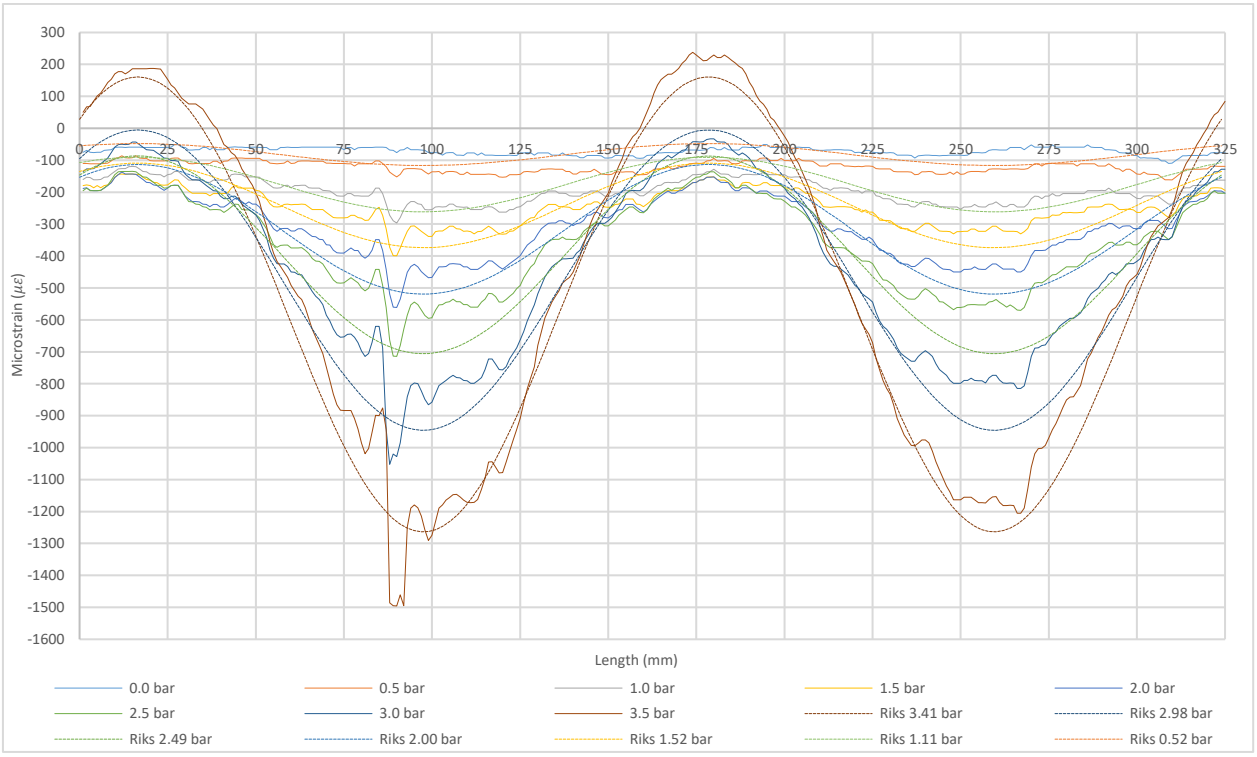

Figure 7 Optical fiber and FEA strain fields for the middle circumference (at 300 mm) of the tube. The dashed curves are from FEA and the continuous lines are from the optical fibers. The curves with equal color are at the same pressure.

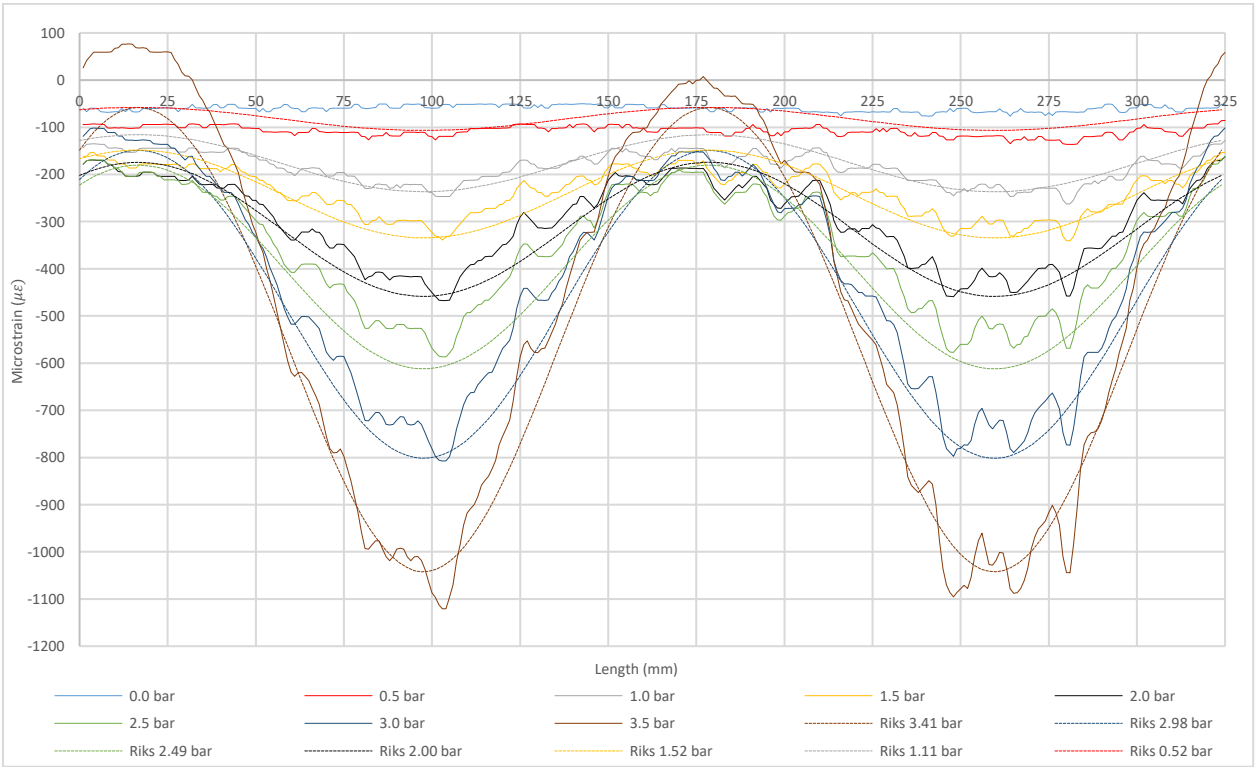

Figure 8 Optical fiber and FEA strain fields for the bottommost optical fiber circumference (at 150 mm) of the tube. The dashed curves are from FEA and the continuous lines are from the optical fibers. The curves with equal color are at the same pressure.

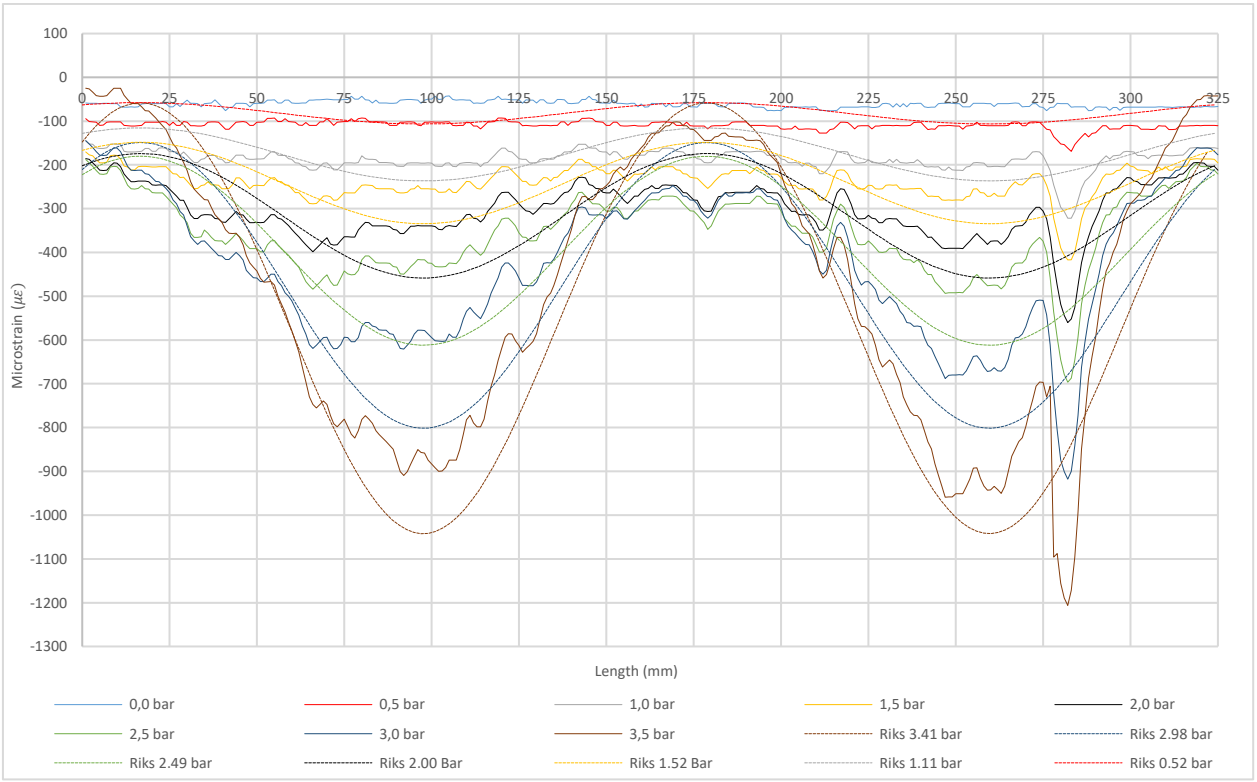

Figure 9 Optical fiber and FEA strain fields for the topmost optical fiber circumference (at 450 mm) of the tube. The striped curves are from FEA and the continuous lines are from the optical fibers. The curves with equal color are at the same pressure.

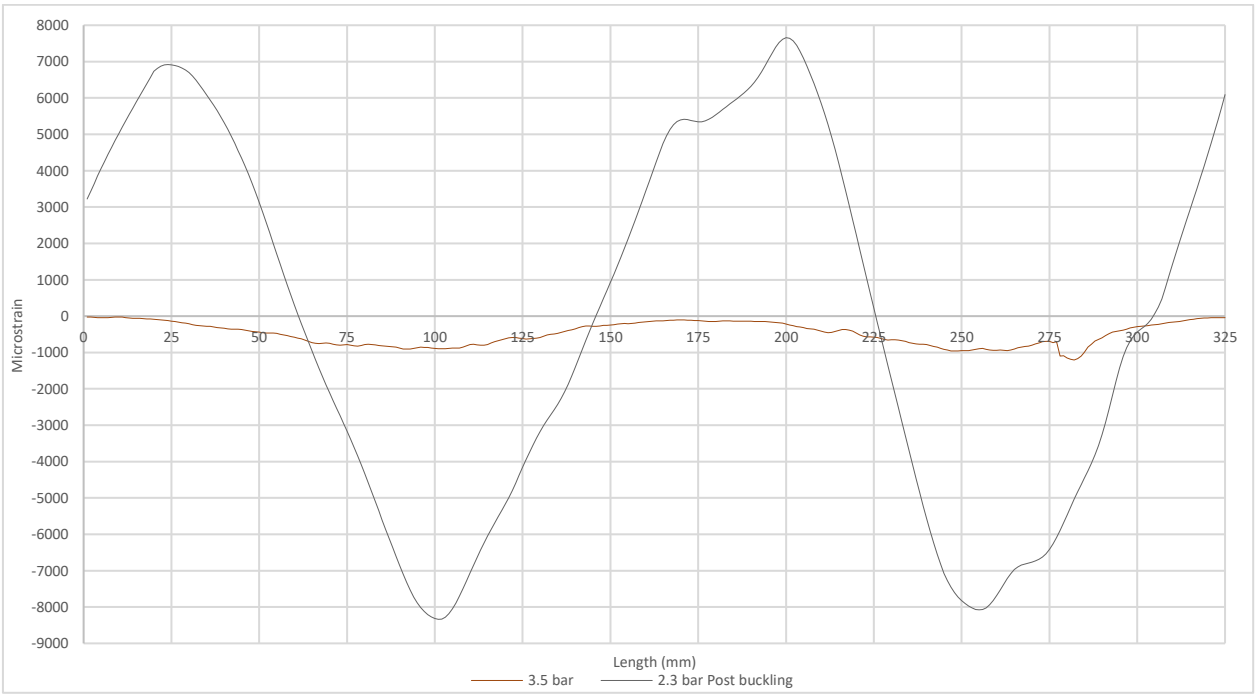

Figure 10 Optical fiber strain field at 2.3 bar from the topmost optical fiber circumference of the tube (450 mm) after occurrence of the pressure dependent leakage, the curve was smoothed due to severe noise. To show the extent of the strain after leakage occurred, the 3.5 bar strain field from before leakage is included.

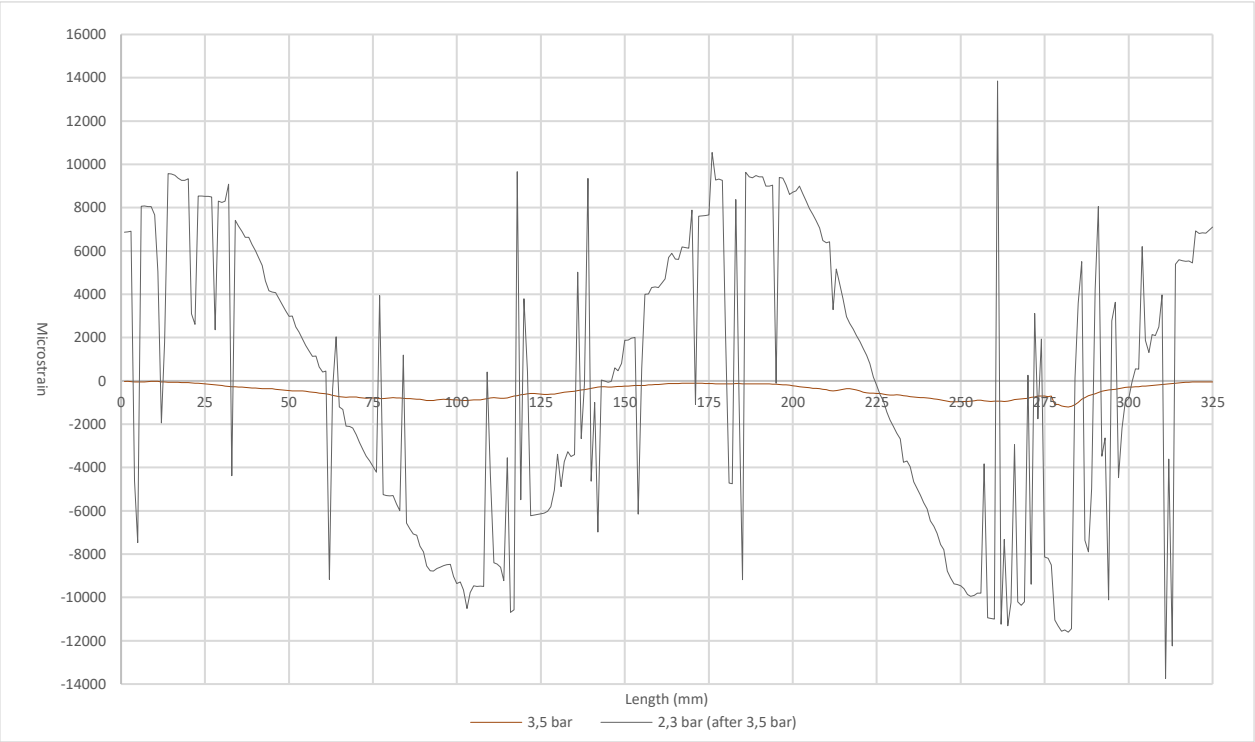

Figure 11 Optical fiber strain field at 2.3 bar from the topmost optical fiber circumference of the tube (450 mm) after occurrence of the pressure dependent leakage, without smoothing. To show the extent of the strain after leakage occurred, the 3.5 bar strain field from before leakage is included.

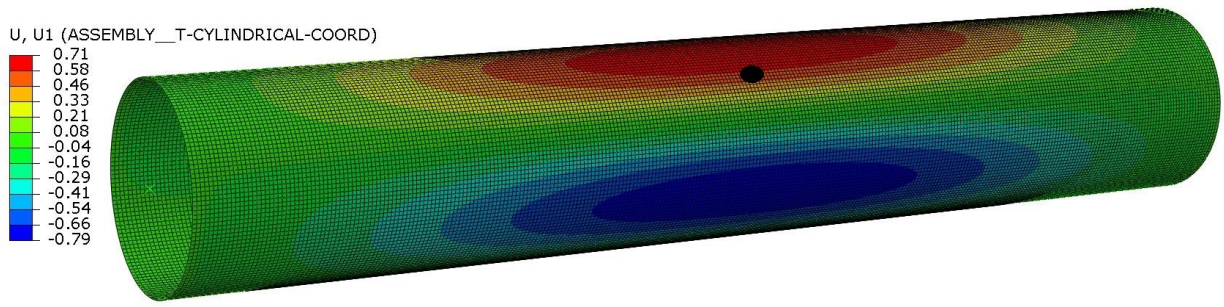

Figure 12 Radial displacement plot at 3.41 bar with a visualization deformation scale factor of 1.0 and units in mm. The black dot is the starting point for the strain field at 300 mm, the starting point for the 150 and 450 mm fields are along the same longitudinal axis. The two-lobe buckling shape is clearly present, with the creases in blue and lobes in red color.

Discussion

In this section, the results will be discussed taking into account possible failure modes causing buckling earlier than predicted by the FEA and comparing the results to other's work.

The FEA and the optical fiber strain fields correlated well up to 3.5 bar, as seen in Figure 7, Figure 8 and Figure 9. The optical fiber strain tends to be slightly lower than the corresponding FEA strain and the average difference is 15% over the areas in the graphs with the most strain (between 50 and 145 mm and 215 and 310 mm along the abscissa axis in the graphs). Assuming that the optical fiber functioned properly, a likely explanation for the deviances can be explained by the modelling approach; elliptical presumption and pinned-constrained connection to the end fittings in the FE model. Unlike the FE model, the tube likely had a varying ovality along the length combined with other imperfections such as slight

differences in layer thicknesses and volume fractions. These are effects that are difficult to estimate and implement in a FE model and it is to be expected that the FE model behave somewhat differently. It is worth noting that the radial displacement at 3.41 bar of -0.79 mm in Figure 12 is in the same order of magnitude as the radial displacement relative to a perfect circle at an ovality of 0.46 %, which is ±0.23 mm. Seeing as these two numbers are of the same magnitude, the idealization of modelling the imperfection in the FE model elliptic is likely present through the pressure range in question.

Maybe contributing more to the strain deviances than the FE model's idealized shape is the fact that the end caps are constrained as pinned. Seeing that the length influences the buckling pressure at a tube length of 600 mm, as shown in the length sensitivity investigation in Figure 2, it matters how they are constrained. The end caps mounted on the tube constrain the tube somewhat and it is an idealized assumption that adds compliance to the FE model when they are pinned. Supporting that the end caps are constrained too compliant is the work done on shorter tubes by E. Hugaas [16]. Hugaas found that for shorter tubes with comparable geometry, the end caps had to be constrained as fixed to achieve good correlation when using ovality as the matching parameter. The likely best way to model the end caps would be to introduce springs in the FE model. Though springs are a more correct representation of the actual constraints, this would add complexity and be yet another parameter that had to be tuned with the experiments to be correct. Additionally, the precisely machined end caps will enforce the ends to remain circular, while the model assumed a constant ovality along the length. Even though the FE model could have been refined to more closely resemble the actual tube and the constraints, the ovality is a good general representation of the tube's imperfections. Though the ovality was tuned to the optical fiber strain fields, the resulting correlation is so good that the FEA acts as a step in verifying the functionality of the OBR 4600 for submerged composite tubes.

As can be seen in Figure 8 and Figure 9, the bottommost (150 mm) optical fiber strain field show noticeably more strain than the equivalent topmost (450 mm) strain field. This can be due to uneven application of sealant on the end caps or imperfections on the tube close to the ends giving differences in the end constraints. Applying sealant and end caps evenly between top and bottom is a controllable parameter and was as far as possible attempted. The imperfections close to the ends of the tube are however difficult to control and can possibly be the main reason for the strain difference between the 150 and 450 mm strain fields.

The leakage initiated just above 3.5 bar was likely caused by matrix microcracks resulting in delamination allowing water to penetrate all the layers. Delamination and matrix microcracking, as opposed to fiber breakage, can be hard to spot in an unstrained sample if the extent of the damage is small. However, the extent does not have to be large in order to reduce the mechanical properties of the laminate [22], causing buckling at 3.5 bar instead of at 4.33 bar for the failure free FEA tube. Indicating that buckling actually occurred is the very high strains in the post-leakage 2.3 bar strain field in Figure 10. Assuming buckling, the extensive noise in the raw 2.3 bar strain field evident in Figure 11 was likely caused by high strains during buckling combined with matrix cracking in the top ply, damaging the fiber. M. Pinto et. al. [7] observed the same effect. Pinto tested 279.4 mm long tubes of 1.52 mm thickness and 60.3 mm and 76.2 mm inner diameter with a layup of $[\pm 15°, 89°, \pm 45°, \pm 15°]$, resembling the layup used in this paper. The tubes, though made of CFRP, buckled at comparable pressures of 7.3 bar (76.2 mm ID) and 16.0 bar (60.3 mm ID). Pinto observed extensive deformations during buckling to the extent where the adjacent walls of the tubes contacted. The extensive deformations reported by Pinto may explain the high strains in the post buckling strain field. The 76.2 mm ID tube returned close to its original shape after depressurizing, though with visible matrix cracks. The other tube suffered more catastrophic failure. Due to a smaller length to diameter ratio, the 76.3 mm ID tube buckled as three lobe, instead of two lobe as for the 60.3 mm ID tube.

Further supporting leakage from non-visible failure from matrix cracking and delamination is the work done by E. Hugaas [16]. Hugaas tested tubes of comparable geometry with the same end caps and testing equipment, but with a more optimized layup. Hugaas investigated matrix cracking from a failure theory point of view and found it likely that matrix cracking and delamination had occurred in both the tube tested in this paper and in the optimized layup tube. High deformations close to the end caps during buckling could also have contributed to the leakage.

Though the post-leakage reading contains comparably more noise than the pre-leakage readings, the pre-leakage strain fields are not as smooth as they should be. Since the zero strain fingerprint was read before the tube was submerged, the pre-leakage noise is likely either a result of rough handling causing fiber damage when placing the tube in the autoclave or due to processes occurring after the tube was submerged. Seeing as great care was taken while placing the tube in the autoclave, it is likely the latter that caused the noise. Though the tube was sanded before the fiber was applied, some roughness was still present so as not to reduce the wall thickness by too much. When pressure was applied, the fiber would be forced into the still present rough areas and the noise would be expected to increase with increasing pressure. Looking at the graphs, the noise can be seen to follow the mentioned theory. A good example of this can be seen between 275 mm and 290 mm in Figure 9, where there is a pronounced peak in compressive strain that steadily increases with increasing pressure. Besides and also due to the roughness it is also possible that the upper layer stretched and compressed unevenly, contributing to the “noise”. Additionally, fiber damage would yield a more constant noise with a more distinct pattern, such as for the post-leakage strain field seen in Figure 11. Assuming the noise in the pre-leakage strain fields is caused by the tube’s roughness and variations in compression and tension over the upper layer, categorizing it as natural variations in strain is more correct than calling it noise as such. In this particular case it is fairly clear that the strain fields should be smooth and should not show peaks. The peaks influence the average difference between the FEA and the optical fiber strain fields of 15 % mentioned above. Smoother curves would for most of the strain fields contribute to less average difference. When analyzing components with stress concentrations the smoothening of strain curves becomes more critical and the interpretation more difficult.

An aspect of the results, which is important to take into account for application to longer tubes, is the dependency of the tube’s length for the buckling behavior. Since the tube failed before the predicted buckling pressure in both the Riks analysis and the linear buckling analysis, it is hard to tell whether the length sensitivity investigation that was carried out is correct. More research has to be done so that test results for short tubes can be extrapolated to also be valid for longer tubes, which greatly cuts costs and labor related to verification and testing of long tubes.

The work presented here was done on composite tubes. The optical monitoring system should work equally well on any material, provided the fibers can be bonded well to the surface. This means the optical fibers could function as health monitoring systems on submerged pure polymer or metal tubes as well.

Conclusion

Optical fibers glued to the outer surface of a filament wound tube subjected to external pressure were found to be a very applicable method for monitoring the strains on the tube by utilizing the Rayleigh optical backscattering with the OBR 4600 equipment from Luna Technologies. Utilizing the Rayleigh optical backscattering has the advantage over other strain measurement technologies that strain fields are monitored instead of strain at single points. Therefore, using optical fiber on submerged structures can give a very complete picture of the deformations on pair with visual inspection during testing. In addition

to giving good results for post-processing and analyzing of the behavior, live monitoring of the strain is also possible using the OBR 4600 equipment.

The optical fiber strain fields correlated very well with strain fields from FEA during build up of pressure. The FEA was of a corresponding tube in Abaqus/CAE 6.12-1 using the Riks analysis method. The good correlation was achieved through having the tube in the FEA modeled with a slight elliptic shape with 0.46 % of the nominal diameter of the tube added and subtracted to the major and minor diameter of the ellipse respectively.

Though the strain fields correlated well with FEA during build of pressure, the buckling pressure deviated from the FEA buckling pressure due to early material failure in the tube. The tube buckled at just above 3.5 bar due to a stiffness reduction from material failure, while the FEA predicted buckling at 4.33 bar assuming no material failure. After the failure and buckling occurred, the preceding optical fiber strain fields contained a lot of noise, likely due to high strains during buckling combined with matrix cracking on the outer surface causing fiber damage. However, the optical fibers were able to detect and characterize the failure, making them a good inspection method for the laboratory and possibly for health monitoring in the field.

The Rayleigh optical backscattering should be an applicable method to monitor potential buckling of composite tubes and tubes made of other materials provided that the optical fibers can be well bonded to the surface.

Acknowledgements

The work and results described in this article would not be possible without access to NTNU's laboratories and equipment.

Bibliography

[1] D. Choqueuse and P. Davies, "Durability of Composite Materials for Underwater Applications," *Durability of Composites in a Marine Environment, Solid Mechanics and Its Applications 208,* 2014.

[2] S. T. Peters, Composite Filament Winding edited by S.T. Peters, ASM International, 2011.

[3] DNV GL, DNV GL Recommended practice: DNVGL-RP-F119 Thermoplastic composite pipes, December 2015, DNV GL, 2015.

[4] DNV-GL, DNV Standard DNV-OS-C501. Composite Components, DNV-GL, 2013.

[5] P. Davies, D. Choqueuse, B. Bigourdan and P. Chauchot, "Composite Cylinders for Deep Sea Applications: An Overview," *Journal of Pressure Vessel Technology, Volume 138, Issue 6,* 18 Jul 2016.

[6] P. Davies, D. Choqueuse, L. Riou, P. Warnier, P. Jegou, F. Bigourdan and P. Chauchot, "Composite Materials for 6000 Meters Depth," in *French Composite Materials Conference*, Paris, 1996.

[7] M. Pinto, G. Sachin and A. Shukla, "Study of implosion of carbon/epoxy composite hollow cylinders using 3-D Digital Image Correlation," *Composite Structures Volume 119,* pp. 272-286, 2015.

[8] D. Choqueuse, B. Bigourdan, A. Deuff, B. Douchin and L. Quetel, "Hydrostatic compression behaviour of steel-composite hybrid tubes," in *ICCM17 - The 17th International Conference on Composite Materials*, Edinburgh, 2009.

[9] K. Lim, L. Wong, W. K. Chiu and J. Kodikara, "Distributed fiber optic sensors for monitoring pressure and stiffness," *Structural Control and Health Monitoring,* pp. 303-314, 15 July 2016.

[10] 3B Fibreglass, HiPer-Tex W2020 Rovings Datasheet, 3B Fibreglass, 2009.

[11] Momentive, Technical Datasheet EPIKOTE Resin MGS RIMIR 135 and EPIKURE Curing Agent MGS RIMH 134-RIMH 137, Momentive, 2006.

[12] ASTM, ASTM Standard D3171 - 15 Standard Test Methods for Constituent Content of Composite Materials, ASTM, 2015.

[13] P. Giovanni, Numerical and Experimental Investigation of Impact Behaviour of GFRP Composites (PhD thesis), Trondheim: NTNU - Norwegian University of Science and Technology, 2014.

[14] Dassault Systèmes, Abaqus Analysis User Manual, 6.2.4 Unstable collapse and postbuckling analysis, 2012.

[15] M. Zhao, "On Nonlinear Buckling and Collapse Analysis using Riks Method," in *Abaqus User Conference*, 2008.

[16] E. Hugaas, Optimize Resistance to buckling under external hydrostatic Pressure of thin walled Composite Tubes (Master thesis), Trondheim: NTNU - Norwegian University of Science and Technology, 2014.

[17] D. Samiec, "Distributed fibre-optic temperature and strain measurement with extremely high spatial resolution," *Photonik international,* 2012.

[18] A. Güemes, A. Fernández-López and B. Soller, "Optical Fiber Distributed Sensing - Physical Principles and Applications," *Structural Health Monitoring, Volume 6,* pp. 461-470, 2010.

[19] M. L. Håheim, Health monitoring of Composites using Optical Fibers (Master thesis), Trondheim: NTNU - Norwegian University of Science and Technology, 2012.

[20] J. H. L. Grave, M. L. Håheim and A. T. Echtermeyer, "Measuring changing strain fields in composites with Distributed Fiber-Optic Sensing using the optical backscatter reflectometer," *Composites Part B - Engineering,* pp. 138-146 , 2015.

[21] M. Mulle, F. Collombet, Z. Rédouane, P. Olivier and Y.-H. Grunevald, "Thermal expansion of carbon–epoxy laminates measured with embedded FBGS - Comparison with other experimental techniques and numerical simulation," *Composites: Part A,* 2007.

[22] J. A. Nairn, "Matrix Microcracking in Composites," *Polymer Matrix Composites*, 2000.